Interfacial Structure and Strain Accommodation in Two-Phase $NbCo_{1.2}Sn$ Heusler Intermetallics

Y. M. Eggeler*, E. E. Levin, F. Wang, D. A. Kitchaev, A. Van der Ven, R. Seshadri, T. M. Pollock, D. S. Gianola

Materials Department and Materials Research Laboratory, University of California, Santa Barbara, CA, USA.

*Corresponding author: yolita@ucsb.edu

Abstract:

Multiphasic intermetallic materials are attractive candidates for functional applications where the constituent phases alone do not meet the property targets. The interfaces at the phase boundaries in these materials are central to their macroscopic properties, with the details of the atomic structure underpinning local thermomechanical, electrical, and magnetic behavior. Here, we characterize the interface structure in the biphasic Nb-Co-Sn system consisting of $NbCo_2Sn$ full Heusler (FH) precipitates embedded in a NbCoSn half Heusler (HH) matrix, which exhibits semi-coherent interfaces with a 3.3% lattice parameter misfit that determines the constitution of the FH/HH interface on the nanometer scale. We use detailed transmission electron microscopy (TEM) and atomistic calculations to precisely determine the dislocation content and structure at the semi-coherent interface, which modulates the strain fields in a semi-regular pattern. We find that the interface forms regularly spaced paired partial dislocations with a joint Burgers vector of a/2<110>, favored by misfit energy relief and chemical ordering. The interface exhibits numerous interface steps (disconnections) which in turn determine the precipitate morphology. Overall, the two phases show full coherency except in the vicinity of the misfit dislocation cores located every 11 nm, leading to a modulated strain field parallel to the interface, and no long-range strain fields as the interfacial dislocations accommodate the misfit strain.

Introduction

Heusler compounds (HC) are a versatile class of ternary intermetallics frequently found with a chemical formula XYZ (Half-Heusler) or XY_2Z (Full-Heusler) where X and Y are typically transition metals and Z is a main group element [1]. The FH phase is comprised of four interpenetrating fcc lattices and the HH phase of three, with half of the tetrahedral sites of the HH phase vacant. By tailoring chemical composition, one can control valence electron count

and thus tailor the functional properties of HCs with relative ease [1]. Furthermore, certain compositions produce two-phase microstructures, where a precipitate-phase is embedded in a matrix phase. The interfaces found at the phase boundaries can generate large local strains and strain gradients, which can mediate physical phenomena and ultimately provide an additional means to tailor functional properties. Of particular interest are instances where the interfaces elicit behaviors that are not otherwise hosted by each constituent phase alone. This phenomenon has been recently explored in two-phase Heusler thermoelectric, M-Ni-Sn (M = Hf, Zr, Ti) [2,3,12–14,4–11], and Nb-Co-Sn[15–17], where it is believed that a high density of semicoherent interfaces at phase boundaries increase the number of phonon scattering centers, thereby improving thermoelectric performance. These findings have triggered an interest in understanding and controlling the evolution and constitution of interfaces within two-phase Heusler microstructures, concerning precipitate morphology, size, and volume fraction [2,5–7,15]. Detailed microstructure evolution characterization has up to now been performed for the Ti-Ni-Sn HC two-phase system, where the two-phase microstructure consists of $TiNi_2Sn$ FH precipitates embedded in TiNiSn HH matrix, exhibiting a lattice misfit δ of 2.5%.

The coherency and morphology of matrix precipitates are controlled by a balance of elastic energy accumulation, interfacial energy, and the formation of interfacial misfit dislocations. When a strained layer grows with a coherent interface, the elastic strain energy increases in proportion to the volume but can be accommodated by the introduction of interfacial crystal dislocations at the interface. These misfit dislocations enable the lattice to reduce the elastic energy below a threshold value or to return to a stress-free state [18]. A review by Y. Kimura and Y-W. Chai [4] summarizes how two-phase microstructures in Heuslers evolve after various heat treatments. Their studies suggest that the formation of FH precipitates in the HH matrix may be compared to the well-known formation of Guinier–Preston zones in Al-based alloys [4]. FH nano precipitates initially form within the HH matrix through spinodal decomposition. They evolve from coherent nanoparticles at sub-10 nm scales to coherent nanodisks, followed by coherent platelets, which continue to evolve into semi-coherent platelets and ultimately, semi-coherent spheres beyond sub-μm sizes. The HH/FH-interface transitions from coherent to semicoherent as precipitates grow larger, and the stored elastic energy is accommodated by interfacial misfit dislocations[4].

The detailed structure and chemistry of interfaces in multiphasic HCs can thus adopt a diversity of forms across many length scales, and consequently, play a large role in influencing macroscopic properties. The focus of our study is the microstructure and interfacial structure

of biphasic $NbCo_{1.2}Sn$, wherein the FH $NbCo_2Sn$ precipitates have already evolved to semi-coherent spheres on the sub-10 μm scale within the HH NbCoSn matrix [15]. As the FH precipitates are ferromagnetic at low temperatures, this system is of particular interest as it has been recently proposed that magnetic Heusler materials may exhibit exotic magnetic phases when large strain gradients characteristic of semi-coherent interfaces locally disrupt their usual crystal symmetry [19]. Here we present a detailed characterization of the structure of the semi-coherent FH/HH interface and the accompanying strain field as a step towards developing Heusler biphasic materials exhibiting exotic strain-controlled properties.

Experiments:

A detailed description of the processing of these Heusler compounds is given by Buffon *et al.* [15]. In short, elemental Nb (Aldrich, foil, 99.8%), Co (Aldrich, pieces, 99.5%), and Sn (Aldrich, shot, 99.8%), were weighed out with the stoichiometry $NbCo_{1.2}Sn$ and processed using a Crystalox MCGS5 induction levitation melting system equipped with a water-cooled copper crucible. The 15 g ingot was melted twice to ensure homogeneous mixing. Pieces from the resulting button were encapsulated and evacuated in fused-silica ampoules, which were then exposed to a further heat treatment at 800°C for 6 days without oxidation. Cylinders of 3 mm diameter were cut from the buttons using electrical discharge machining (EDM), which were then sliced with a disc saw into discs of about 1 mm thickness. The discs with a 3 mm diameter were then mechanically ground and polished to a thickness of 0.12 mm before final thinning using a twin-jet electropolisher in a solution of 92.5% methanol and 7.5% perchloric acid by volume. The electrolyte was cooled with liquid nitrogen to a temperature of –50°C to –40°C, and polishing was performed at 16–18 V and 20–28 mA.

The microstructure was first analyzed using scanning electron microscopy (SEM) (FEI Apreo S). For a detailed investigation of the precipitate/matrix interface, site-specific focused ion beam (FIB) preparation using an FEI Helios Dualbeam Nanolab 600 was applied perpendicular to the long axis of the precipitates to obtain transmission electron microscopy (TEM) samples. TEM was used to characterize the micro- and nanostructure of the two-phase HC. High-resolution scanning transmission electron microscopy (HRSTEM) images were acquired using an FEI Titan 80-300kV operating at 200 kV. A transmission electron microscope of type FEI TALOS F200X S/TEM with an integrated ChemiSTEM unit using a SuperX detector for high-efficiency energy dispersive x-ray spectroscopy (EDXS) operating at 200kV was used to

chemically identify, the two-phase Heusler samples. Strain mappings on the atomic scale were realized by acquiring HRSTEM images and digital post-processing based on Fast Fourier transform algorithms incorporated within the Digital Micrograph software by GATAN. The geometric phase analysis (GPA) is a digital signal processing method used with Fast Fourier transform algorithms to quantify displacements and strain fields in crystalline lattices at nanoscale resolution developed by Koch *et al.* [20,21].

Density functional theory (DFT) calculations of the γ-surface energy were performed using the Vienna Ab-Initio Simulation Package (VASP) [22] and the multishifter code package [23]. Since in this case, the relevant dislocations terminate at the FH/HH phase boundary, the slab supercells were constructed with a HH vacancy ordering on the Co sublattice on one side of the interface, and the FH phase on the other. Thereby, the interfacial γ-surface we obtain captures the chemical energy of a coherent FH/HH interface, at a lattice parameter that is the average of the equilibrium FH and HH structures. While the elastic energy associated with the interfacial strain is a significant fraction of the total interfacial energy, it does not contribute to the interfacial γ-surface as all relative translations of the FH/HH phases have the same strain.

All surface slab supercells were chosen such that the supercell contained at least 3 unit cells of each phase along the surface normal direction to minimize spurious cross-slab interactions. The γ-surface energy was calculated using 9x9, 9x5, and 9x9 grids for the (100), (110) and (111) planes respectively, optimized at each point over slab separation distance. DFT calculations were performed using the Perdew-Burke-Ernzerhof exchange-correlation functional [24] projector-augmented wave method with a reciprocal space discretization of 400 K-points per $Å^{-3}$, ensuring that all slab calculations of the same surface had identical k-point grids and that total energies were converged to 10^{-6} eV.

Results:

Scale-bridging microstructural characterization is key to understanding the structure-property relationships in functional Heusler intermetallics, especially in two-phase Heusler microstructures where the precipitate phase is misfitted into the matrix phase. Accordingly, the precipitate morphology and interfacial structure are highly dependent on the lattice misfit between the precipitate and matrix phases. In the first part of this paper, we discuss the micrometer-scale features of the microstructure (precipitate morphology, distribution, and coherency). In the following sections, we focus on the microstructure to the nanometer scale and finally the atomic structure of the interfaces.

Precipitate morphology

After solidification and heat treatment, the intragranular microstructure of $NbCo_{1.2}Sn$ consists of a homogenous distribution of the FH precipitates in the HH matrix (Figure 1a). Table 1 lists the matrix and precipitate composition, which were measured by STEM EDXS. Concerning the nominal ingot composition of $NbCo_{1.2}Sn$, the precipitates comprise 20% of the volume, in agreement with the fraction of bright (Figures 1 b and d) or dark (Figure 1c) regions evaluated by image analysis.

Table 1: Composition of each phase as determined by STEM EDXS.

Phase	**Nb [at.%]**	**Co [at.%]**	**Sn [at.%]**
FH phase (STEM EDXS)	26.5	49.9	23.7
HH phase (STEM EDXS)	34.0	34.4	31.7

As can be seen from the results presented in Table 1, the precipitate and matrix composition adopt respectively the expected full (1:2:1) and half (1:1:1) Heusler compositions with less than 2 at.% deviation, within the error of the EDXS measurement.

In Figure 1b a grain boundary is indicated by a dashed white line, and the FH precipitates appear to have different shapes in the two grains at different orientations. In the top grain, we can see the long axis of the ellipsoidal-shaped precipitates (similar precipitate shapes are reported by Kimuro et al. [18]), highlighting their high aspect ratio. The long axis can extend to more than 10 μm and the short axis is in the range of 500 nm, shown in the magnified high angle annular dark field (HAADF) STEM images acquired after having oriented the sample in zone axis in Figure 1c and d, respectively. The unit cells of the FH and HH phases are schematically shown in the inset of Figure 1d. The cube-on-cube orientation relationship of the HH matrix and the FH precipitates is evident from the formation of a stretched Moiré pattern in the TEM images taken from the regions where the two phases overlap in the TEM foil. Two types of Moiré patterns can be differentiated, first, a rotational Moiré pattern where one lattice is rotated with respect to the other lattice, and second, a stretched Moiré pattern where the phases share a common orientation but have different lattice parameters [25]. The varying contrast within the precipitates arises from alternating regions of pure FH phase and extended regions where HH and FH phases overlap, Figure 1e. This indicates the presence of inclined

interfaces. Enlarging one of these regions reveals a regularly arranged dot pattern with a threefold symmetry, as shown in Figure 1e. The inset in Figure 1e shows this dotted pattern enlarged represents a stretched Moiré pattern, arising from equally oriented overlapping FH and HH phases with different lattice parameters [26]. This is confirmed by the complementary selected area electron diffraction (SAED) pattern of zone axis [111] shown in Figure 1f. Close inspection of one of the six <220> diffraction spots (Fig. 1f inset) shows splitting spots, as expected from the two phases with an orientation relationship but exhibiting different lattice sizes. The spot closest to the direct beam belongs to the FH phase, which has a larger lattice parameter compared to the HH phase. A lattice misfit δ of 3.3% is obtained by measuring the FH/HH spot separation distance, which is in agreement with the lattice parameter values from previously reported XRD measurements [15]. Furthermore, these complementary observations prove that the phases share a common orientation with a distinct cube-on-cube orientation relationship. Therefore, the origin of the Moiré pattern shown in Figure 1e is related to the difference in lattice constants, and not to a rotational shift between the two phases.

The region shown in Figure 1 e is imaged along the <111> zone axis, so a dominant hexagonal dot Moiré pattern is created. The stretched Moiré spacing, $D_{Moiré}$, can be derived from equation 1 [27] using the lattice parameter **d** for the {110} planes for the FH and HH phase respectively:

$$D_{Moiré} = \frac{\boldsymbol{d}^{\boldsymbol{FH}}_{[\mathbf{110}]} \cdot \boldsymbol{d}^{\boldsymbol{HH}}_{[\mathbf{110}]}}{\left|\boldsymbol{d}^{\boldsymbol{FH}}_{[\mathbf{110}]} - \boldsymbol{d}^{\boldsymbol{HH}}_{[\mathbf{110}]}\right|} = \quad 13.01 \text{ nm} \qquad \text{(eq.1)}$$

The value agrees with the distance measured in Figure 1e. Note that the spacing of the Moiré pattern is also close to the misfit dislocation spacing as discussed later (in Figure 2), which could easily lead to misinterpretation of the contrast. At controlled crystallographic defect STEM image conditions used in this work for Figure 1, the contrast of the stretched Moiré pattern dominates that of the misfit dislocation network. Due to the large misfit, the precipitates are semi-coherently embedded in the matrix, which implies a high misfit dislocation density on the submicron scale. It seems reasonable to assume that the high coherency strains in combination with elastic anisotropies in the system result in precipitate faceting on the micrometer scale.

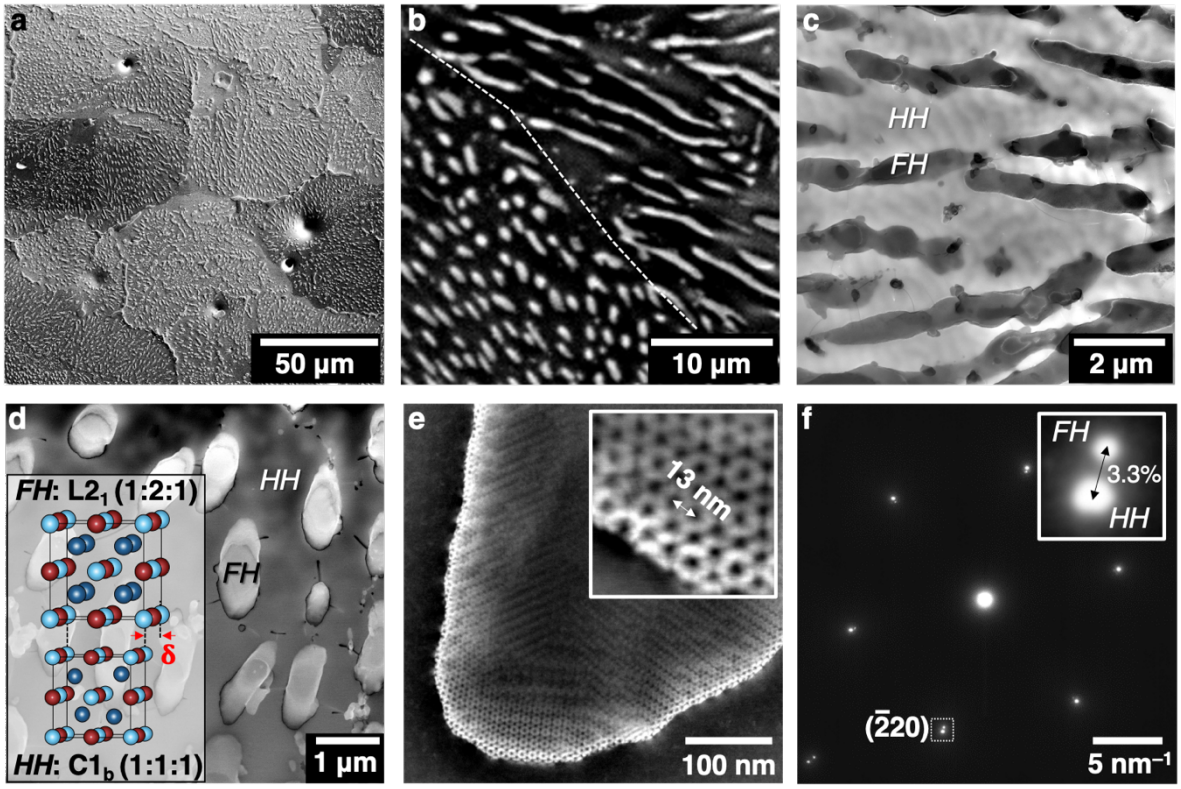

Figure 1: The two-phase microstructure of the $NbCo_{1.2}Sn$ full Heusler (FH) / half Heusler (HH) compound. (a) SEM overview image of the $NbCo_{1.2}Sn$ alloy demonstrating the homogenously distributed precipitates after solidification and heat treatment. (b) STEM image highlighting a grain boundary between HH grains. The precipitates exhibit an ellipsoidal-shaped morphology with a high aspect ratio. STEM micrographs of the long precipitate axis and the short precipitate axis are depicted in (c) and (d) respectively. A sketch of the FH and HH unit cells and their expected lattice misfit δ with respect to each other is shown in the inset of (d). (e) A region where FH and HH phases, both oriented in the [111] zone axis, are superimposed, creating a hexagonal Moiré pattern due to their mismatched lattice parameters, shown enlarged in the inset. (f) The selected area electron diffraction pattern of the [111] zone axis shows splitting of the fundamental reflections confirming the different lattice parameters of the phases involved.

Interface coherency

We now focus our attention on the HH/FH interface to elucidate its general structure and the associated strain distribution. For this analysis, we perform a site-specific FIB lift-out perpendicular to the long axis of the precipitates as depicted in Figure 2a. The high-resolution investigation was carried out at the very thin edge of the lamella, indicated by a red rectangle,

to minimize any effect of the inclined interface. This rectangular area is shown enlarged in Figure 2b, as imaged along the [110] zone axis using high resolution HAADF-STEM.

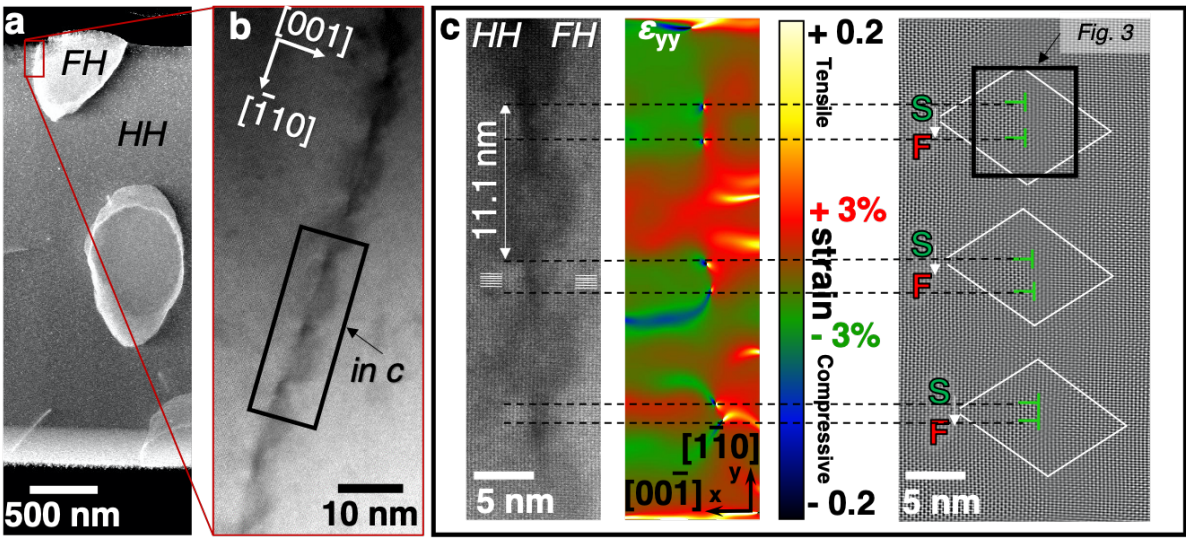

Figure 2: (a) STEM image of the FIB lamella with foil normal parallel to the [110] direction of the HH phase (foil normal, see Figure 2b). The interfacial region is highlighted by the red rectangle. (b) STEM micrograph showing an alternating contrast along the HH/FH interface. The region encircled by a black rectangle is further investigated in (c). (c) HRSTEM image of the interface showing atom columns oriented in [110] zone axis which is digitally post-processed with FFT based GPA. The GPA map reveals the interface strain distribution and shows paired hot spots indicating dislocations every 11 nm along the interface. Burgers vector circuits using the right hand / start (S) to finish (F) (RH/SF) convention are performed in the corresponding IFFT image of the HRSTEM image along the <111> directions. Note that GPA strain is measured with respect to the HH phase, meaning that even at equilibrium, the FH phase appears as a region of expanded lattice parameter, i.e. tensile strain.

Strain maps of the interface reveal the presence of interfacial dislocations, owing to the 3.3% smaller lattice parameter of the HH phase compared to that of the FH phase. Specifically, the HRSTEM image of the HH/FH interface depicted in Figure 2c reveals a regular contrast pattern along the interface where darker concentrated regions alternate with lighter regions. From this image, we quantify the strain distribution around the interface using geometric phase analysis (GPA) [28], with the HH lattice as the strain-free reference. The darker and lighter contrast variations in the HRSTEM images can thereby be attributed to strain variations along the interface. Within the concentrated darker regions (Figure 2c), the corresponding ε_{yy} map

reveals closely spaced paired zones with concentrated strain fields (i.e. hot spots), where a tensile strain field opposes a compressive strain field.

The 10 nanometer wide regions in between (lighter regions in HRSTEM image) exhibit lower and more evenly distributed strain values varying around +/- 3%, in agreement with the misfit strain. These are the regions where the lattices of the FH and HH phase are constrained and template coherently, whereas the coupled hot spots indicate the presence of dislocations serving to accommodate the elastic strain energy. The ε_{yy} map indicates that the compressive strain field regions of the hot spots reside within the HH-phase, suggesting that the extra inserted half-planes (feature of edge dislocation) exist in the HH-phase. It is important to note that the sign of the GPA strain field across the interface depends on the choice of the strain free reference area, which in the case of Figure 3c was chosen to be in the HH lattice. With respect to the HH lattice, the FH phase has a larger lattice parameter and will be identified by GPA as an expanded lattice compared to the reference, i.e. tensile strain. Thus, while the GPA map represents the FH phase globally as a region of tension, the reality is simply that this is a region with a larger equilibrium lattice parameter with deviations from the ideal case due to thin foil relaxation effects. Within this background, misfit dislocations create hot spots at the interface GPA map, where an irregular tensile strain on the FH side and compressive strain on the HH side can be observed. Finally, a curious feature is that in contrast to a coherent interface, where it is known that the larger lattice parameter phase is in compression and the smaller lattice parameter phase in tension, the semi-coherent interface investigated here shows the opposite due to the close spacing of the misfit dislocations: locally the larger FH lattice is expanded and the smaller HH lattice is compressed.

Further analysis of the HRSTEM images provides details of the misfit dislocations (MDs) formed at the interface. To accommodate the 3.3% misfit at the interface in the HH/FH NbCo1.2Sn two-phase system, these dislocations are introduced in the HH phase to accommodate the smaller lattice of the HH phase. As evidenced by the GPA map, dislocations line up in a regular pattern along the interface approximately every 11 nm. To locate the dislocations in the HRSTEM image and in the filtered inverse fast Fourier transform (IFFT) image, superimposed horizontal dashed black lines are drawn and aligned with the hot spots to guide the eye. Burgers circuits are drawn using the right hand (RH) convention indicated by white lines in the filtered IFFT image of Figure 2c and the Burgers vector which represents the closure vector of the circuit, is then drawn from the Start to Finish (S to F) points of the circle. Using the right hand start to finish (RH/SF) convention [29] we analyze the Burgers vector of

the pair of dislocations, which reveals a $\boldsymbol{b_{pair}}$ of a/2[-110] for the paired dislocations, which is in agreement with reported Burgers vectors for MDs in two-phase half Heusler composites [5].

An equilibrium MD spacing can be estimated as $D_{MD} = \frac{\boldsymbol{b_{MD}}}{\delta} = 12.6\ nm$, using the HH lattice parameter a_{HH} = 0.421 nm to give the magnitude of $\boldsymbol{b}_{MD} = a_{HH}/2\langle 110\rangle$, and 3.3% for the lattice misfit δ. The experimentally measured spacing D_{MDexp} between the regions with dislocation pairs shown in Figure 2c is measured to be 11.1 nm, indicating that the interface dislocations largely shield the misfit induced interface strain field on the sub-micrometer scale, although the presence and structure of the dislocation pairs is unique and deserves additional attention.

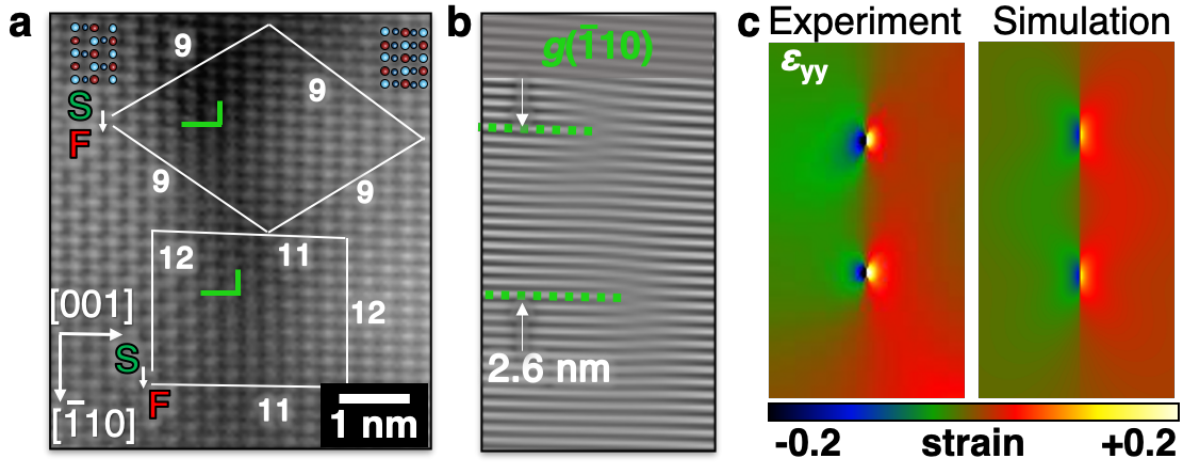

Figure 3: Analysis of the paired partial dislocations. (a) IFFT of the HRSTEM image marked by a black rectangle in Figure 2c, indicating the two dissociated partial dislocations in green. (b) IFFT mask applied filtered for the {-110} planes labeled respectively. Inserted extra half-planes are indicated by dashed green lines. (c) GPA of the interface region shown in (a) revealing two dislocation strain fields, in good agreement with a complementary simulation of two edge dislocations.

Interface dislocation characterization

The misfit dislocations are present as two partial dislocations, with an apparent Burgers vector of a/4[-110], as indicated by green "L" in the HRSTEM image (Figure 3a). While the partial dislocations comprising the a/2[-110] MDs have apparent in-plane Burger's vectors of a/4[-110], the true structure of these dislocations may involve an out-of-plane component. Figure 3a shows an HRSTEM image taken from the encircled black region marked in the IFFT of

Figure 2c. In this image, the two phases can be distinguished as indicated by schematic [110] unit cells of HH (upper left) and FH (upper right). The two lattice discontinuities appear in the Burgers circuits on the image, marked by green dislocation signs and the planes next to them continuously cross the phase boundaries. The Burgers vector circuit, shown in Figure 3a is executed around each dislocation along different crystallographic directions, see top and bottom circuits, respectively. The individual partial dislocations reveal the same Burgers vector of $\boldsymbol{b}_I$ =a/4[-110] independent of the crystallographic directions chosen for the Burgers circuit. As expected for an edge dislocation, the IFFT of the horizontal {-110} planes (Figure 3b) reveals two inserted half-planes, marked in green with a separation distance of 2.6 nm. The inserted half planes in the array of isolated {-110} planes do not terminate on the same vertical (100) plane, which indicates the presence of a step in the interface. It is possible that $\boldsymbol{b}_I$ derived from the Burgers circuit may have an out of plane component (along the foil thickness) that cannot be detected by the Burgers vector circuit, which captures only the in-plane contributions. Hence the measured closure vector $\boldsymbol{b}_I$ of a/4[-110] for both dislocations may be the result of an out of plane projection originating from dislocations of type a/2[-100] and a/2[010]. To confirm that the strain arises from misfit dislocations on the interface we compare in Figure 3c the experimentally derived GPA stain map with theoretical calculations. For the calculations, the Peierls-Nabarro dislocation model was chosen and performed for the identified paired partial dislocations. Although the misfit dislocations are on the HH/FH interface and the strain affects the two different lattices, only the HH lattice is considered for simplicity. Since the extra lattice plane is on the side of the HH matrix to compensate for the misfit with the FH lattice, the lattice parameter and elastic constants of NbCoSn half Heusler phase are used. These are obtained from DFT calculations and are reported in Table 2. Indeed, the experimentally derived ε_{yy} map matches well the theoretically calculated ε_{yy} map confirming that the strain arises from the partial dislocations. Cubic $NbCo_2Sn$ is not stable at low temperatures, and therefore these calculations could not be performed for the FH phase.

Table 2: Elastic constants derived from DFT calculations for the half Heusler (NbCoSn) phase.

	C11 in GPa	C12 in GPa	C44 in GPa	E in GPa	G in GPa	nu	K in GPa
Half Heusler NbCoSn	286	90	60	242	60	0.24	156

Our results indicate that the interface configuration presented in Figure 3 represents the best compromise between chemically enforced order and crystallographic compatibility and the need to minimize overall strain energy, as discussed in detail in the following section. Figure 4a shows the unit cell of the Full Heusler $L2_1$ phase, together with green and red arrows, which represent potential elementary displacement steps of the interface dislocations. Figure 4b shows the projected energy landscape of displacements along the (100) plane, where the two possible displacement vectors (two a/2<100> and two a/4<110>) are shown. These two dissociation scenarios and associated displacements yield significantly different energy pathways, as shown in Figure 4c. A double shift by the a/4<110> vector requires much higher energy than two shifts along perpendicular a/2<100> directions. This fact suggests that that the out-of-plane configuration (red arrows in Figure 4a) with two a/2<100> dislocations represent the energetically favorable configuration and rationalizes our HRSTEM observations.

To illustrate the detailed atomic arrangement at the interface we show a schematic view of the misfit dislocations determined by the HRSTEM analysis (Figure 4d). This perspective gives the following insights: (1) The dislocation cores (red half planes in Figure 4d) terminate in the FH phase. Thus, even though a very thin area was chosen for the HRSTEM investigations, the interface is nevertheless inclined along the foil normal for one or two unit cell distances, which is consistent with the blurred regions in the HRSTEM image of the interface in Figure 3a. (2) While at first glance the two partial dislocations seem to be collinear along [-110], the detailed schematic redraw in Figure 4d reveals that the inserted half-plane finishes on different {001} planes indicated by vertical green dashed lines. This step most likely does not influence the dislocations' structure, but may modify the strain field slightly as reported in previous studies [30]. Accordingly, the schematic redrawing of the interface (Figure 4d) shows that the HH and FH also end at different heights along {001}, denoting the interface step. (3) In between the partial dislocations, the {-110} lattice planes coherently transfer into the adjacent phase.

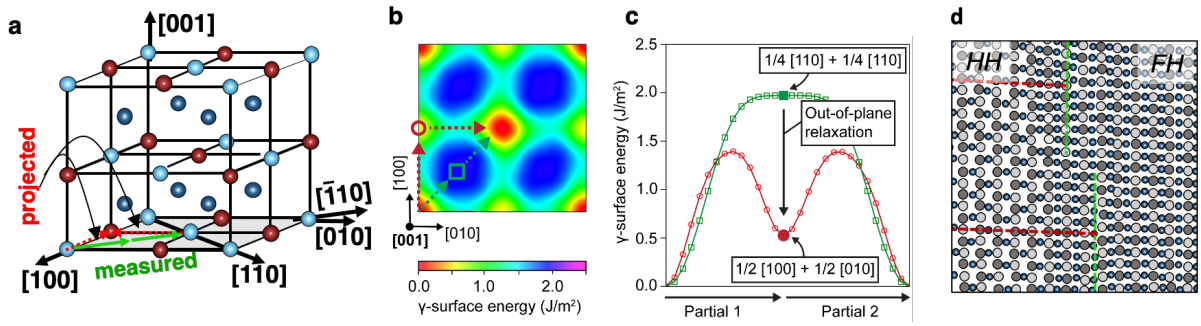

Figure 4: (a) Full Heusler $L2_1$ unit cell including the experimentally found vectors associated with the Burgers vector of the interface dislocations. (b) γ-surface of the {100} FH/HH

interface plane. Arrows indicate the two discussed dislocation dissociation scenarios; green arrows represent the a/2<100> dissociation pathway and red arrow the a/4<110> dissociation. These two scenarios are shown in (c) as interfacial γ-surface line profiles, clearly showing that the a/2<100> + a/2<010> pathway is energetically favorable. The HRSTEM image from Figure 3a is manually redrawn and shown in (d) locating the dislocations (red) and visualizing the interface step (green).

Discussion

The $NbCo_xSn$ system is an interesting model system for studying the impact of interface structure on elasto-magnetocaloric properties. In addition to forming coherent and semi-coherent, highly strained interfaces, the FH precipitates in this system undergo a first-order structural transition (martensitic transformation) and then a second-order magnetic transition during cooling from room temperature. The dislocation structure and resultant strain state at the interface likely impacts both transitions, and thus may be used to manipulate the kinetics of the martensitic forward and reverse transformation, thermal hysteresis, and magnetic behavior.

As a step towards resolving these multi-property couplings, we have investigated the interfacial structure of full-Heusler $NbCo_2Sn$ precipitates embedded in the half-Heusler NbCoSn matrix after a homogenization heat treatment. Our analysis resolves the complete atomistic structure of the misfit dislocations in the late stages of precipitate growth and complements previous work by Y. Kimura and Y-W. Chai [4], which focused on the early stages of precipitate formation.

Our collective results and analysis suggest that paired a/2[-100] and a/2[010] dislocations form during precipitate growth due to large misfit (>3%) related interface energies, that more efficiently relieve elastic energy and satisfy chemical ordering preferences. Our hypothesis is supported by the results derived from the HRSTEM analysis and DFT calculations that show a low energy profile for the [100] dislocations.

Precipitate coherency and misfit dislocation spacing

The $NbCo_{1.2}Sn$ system investigated in this work phase separates into the FH $NbCo_2Sn$ precipitate phase and the HH NbCoSn matrix phase. Buffon et al. [16] measured a lattice parameter of a_{FH}= 0.615 nm and a_{HH}= 0.596 nm, resulting in a lattice misfit of 3.2%, which is in good agreement with the values obtained in this work by SAED (Figure 1f). The differences

can be attributed to thin foil relaxation effects. It is known that in one dimension lattice misfit can be completely accommodated without any long-range strain fields by a set of edge dislocations with a spacing D_{MD} given by equation 1. Paired misfit dislocations with a joint Burgers vector of a/2[-110], the shortest lattice translation vectors preserving chemical order and stacking sequence in the FH and HH, are represented by the sum of the two green arrows in Figure 4a and b.

We also calculate that D_{MD} = 12.6 nm, which is in close agreement with the experimentally measured distance between two dislocation pairs (Figure 2) of 11.1 nm, suggesting that the misfit induced strain fields are mostly accommodated. This result is in agreement with the GPA result in Figure 2c.

The alignment of the two phases at the interface is almost perfectly coherent except around the dislocation cores, where the structure is highly distorted and the lattice planes are discontinuous, see Figure 4d. The HH/FH interface, thus, consists of modulated short-range strain fields on the nanometer scale along the interface of the FH precipitates.

Misfit dislocation formation mechanism

The fact that the interfacial misfit dislocations appear as paired partials distinguishes our result from other misfit dislocation behavior seen for example in epitaxial semiconductor systems [31] and structural superalloys [32,33]. In the first common example, 90° misfit dislocations form by the Lomer-Lock mechanism [18], wherein two 60° dislocations on adjacent {111} planes react to create a 90° misfit dislocation [34]. In systems with a large lattice misfit (>1%), these 90° misfit dislocations are regularly spaced along the epitaxial interface [35]. In another common example of superalloys consisting of γ′-precipitates within a γ-phase matrix, during creep dislocations glide within the γ-phase and deposit dislocation segments at the γ/γ′ interfaces. The segments can react with each other and form a unique interfacial misfit dislocation network [33], relieving the relatively small γ/γ′ lattice misfit (<0.5%). As in our case (misfit 3.3%), these misfit dislocations form in parallel with the formation of the interface during the initial heat treatment of the material when the precipitates grow. However, the NbCoSn/$NbCo_2Sn$ interface is unique in that the misfit dislocations exist as pairs. The end result is an unusual ordered array of isolated pairs of partial dislocations, although it is possible that these partials form a more extended dislocation network which is not resolvable in our TEM data due to the competing Moiré contrast.

Planar fault energies associated with transformation and slip behavior in the $L2_1$ full Heusler phase and the $C1_b$ half Heusler phase have been previously studied [36–39]. It is known that when the antiphase boundary (APB) energies are low, <111> slip dominates. As APB energies become higher with increasing ionic character, <100> slip is favored as noted by Rachinger and Cottrell [40]. The planar fault energies calculated for the FH/HH interface of this system are of the order of 500 mJ/m^2 which is a high value for metallic systems however expected for semi-conductor materials as the HH phase NbCoSn.

It is worth noting that, in contrast to planar faults associated with dislocation dissociations, the dislocations observed here were found directly at the interface of a phase boundary, thereby delineating regions where a change in stacking/order sequence occurs when crossing from the HH into the FH phase or vice versa. An interface step was found between the partial dislocations within regions of full coherency in between the paired dislocations. The proposed dislocations thus suggest no dissociation mechanism correlated with the formation of planar defects. Dislocations with the apparent Burgers vector of a/4[-110] (represented by the two solid green arrows in Figure 4a) correspond to local changes in the atomic stacking sequence, in addition to the changes in chemical order seen in the a/2[100] dislocation. These findings are in good agreement with the γ-surface energy pathway in Figure 4c derived from DFT calculations that show higher energy values for dislocation decomposition of the a/4[-110] directions.

Summary and Conclusions

It has been shown for Heusler materials exhibiting thermoelectric properties, that interfaces in two-phase microstructures elicit behaviors that are not otherwise hosted by each constituent phase alone. It is believed that a high density of semicoherent interfaces at phase boundaries increases the number of phonon scattering centers, thereby improving thermoelectric performance. [4,15] We have investigated semicoherent interfaces separating ellipsoidal FH precipitates from a HH matrix in the Nb-Co-Sn Heusler system by HRSTEM. Arrays of paired dislocations every 11 nm were identified at the interface and agree with calculated misfit dislocation distances. At the atomic scale, the interface dislocations reveal to be present as pairs of individual partials, which has not been previously reported in biphasic Heusler systems. Analysis of our HRSTEM experiments and DFT calculations of interfacial energies suggest that paired a/2[100] and a/2[010] dislocations forms during precipitate growth due to misfit (>3%) related high interface energies, that provide a low energy stress relief pathway and

satisfy chemical ordering energetics. Establishing linkages between the interfacial defect structure, local chemical ordering, and their control via judicious processing pathways, and functional properties such as magnetic phase transitions and thermoelectric response represents an interesting avenue for future work [19].

The following points summarize our main results:

(1) After solidification and heat treatment, ellipsoidal FH $NbCo_2Sn$ precipitates with high aspect ratio homogenously form and distribute within the HH matrix and exhibit a common crystallographic cube-on-cube orientation. The lattice parameters of the FH and HH phases differ substantially, resulting in a large lattice misfit δ of 3.3%. This has two consequences: (a) While imaging the precipitates oriented in zone axis condition, a stretched Moiré interference pattern at inclined interfaces dominates the interface contrast; and (b) a dislocation network forms at the interface to accommodate the large misfit strains.

(2) Along the interface, dislocations are found every 11.1 nm, which is close to the calculated (eq.1) equilibrium misfit dislocation distance of D_{MD} = 12.6 nm. In line with the GPA strain maps, this structure suggests that misfit induced wide range strain fields are largely accommodated. The FH and HH match up plane for plane except for the pairs of dislocations, which means there is a modulated strain field with a periodicity of 11.1 nm. Interestingly, the interface dislocations appear as pairs and exhibit a total Burgers vector of a/2[-110]. The two dislocations comprising the pair are separated by 2.6 nm, suggesting a more efficient misfit relief configuration. The Burgers circuit for both dislocations gives an apparent in-plane Burgers vector of **b**=a/4[-110].

(3) On the basis of DFT HH/FH interfacial γ-surface calculations, the apparent measured Burgers vector is most likely a result of an out of plane projection from dislocations with Burgers vector a/2<100> and a/2<010>. The two individual partial dislocations with a separation distance of 2.6 nm along [-110] suggest a chemically more favorable state. Furthermore, interfacial disconnections can be identified between the two partial dislocations, suggesting that the interface contains many steps, presumably either as a consequence of growth kinetics or the energetics of the interface structure.

Acknowledgment:

The research reported here was supported by the Materials Research Science and Engineering Center at UCSB (MRSEC NSF DMR 1720256) through IRG-1. The research reported here

made use of shared facilities of the National Science Foundation (NSF) Materials Research Science and Engineering Center (MRSEC) at UC Santa Barbara, DMR-1720256. We also acknowledge support from the Center for Scientific Computing from the CNSI, MRL: an NSF MRSEC (DMR-1720256) and NSF CNS-1725797, as well as the National Energy Research Scientific Computing Center, a DOE Office of Science User Facility supported by DOE DE-AC02-05CH11231. The UC Santa Barbara MRSEC is a member of the Materials Research Facilities. Network (www.mrfn.org). Y.M.E. acknowledges the support of the Alexander von Humboldt Foundation through the Feodor Lynen fellowship.

References:

[1] T. Graf, C. Felser, S.S.P. Parkin, Simple rules for the understanding of Heusler compounds, Prog. Solid State Chem. 39 (2011) 1–50. https://doi.org/10.1016/j.progsolidstchem.2011.02.001.

[2] J.E. Douglas, M.P. Echlin, W.C. Lenthe, R. Seshadri, T.M. Pollock, Three-dimensional multimodal imaging and analysis of biphasic microstructure in a Ti–Ni–Sn thermoelectric material, APL Mater. 3 (2015) 096107. https://doi.org/10.1063/1.4931764.

[3] G.D. Stucky, J.E. Douglas, T.M. Pollock, N. Verma, C.S. Birkel, M.-S. Miao, R. Seshadri, V.M. Miller, Phase stability and property evolution of biphasic Ti–Ni–Sn alloys for use in thermoelectric applications, J. Appl. Phys. 115 (2014) 043720. https://doi.org/10.1063/1.4862955.

[4] Y. Kimura, Y.-W.W. Chai, Ordered Structures and Thermoelectric Properties of MNiSn (M = Ti, Zr, Hf)-Based Half-Heusler Compounds Affected by Close Relationship with Heusler Compounds, Jom. 67 (2015) 233–245. https://doi.org/10.1007/s11837-014-1233-3.

[5] Y.W. Chai, Y. Kimura, Microstructure evolution of nanoprecipitates in half-Heusler TiNiSn alloys, Acta Mater. 61 (2013) 6684–6697. https://doi.org/10.1016/j.actamat.2013.07.030.

[6] N. Verma, J.E. Douglas, S. Krämer, T.M. Pollock, R. Seshadri, C.G. Levi, Microstructure Evolution of Biphasic TiNi1+x Sn Thermoelectric Materials, Metall. Mater. Trans. A. 47 (2016) 4116–4127. https://doi.org/10.1007/s11661-016-3549-9.

[7] E.E. Levin, J.D. Bocarsly, K.E. Wyckoff, T.M. Pollock, R. Seshadri, Tuning the

magnetocaloric response in half-Heusler/Heusler MnNi1+xSb solid solutions, Phys. Rev. Mater. 1 (2017) 075003. https://doi.org/10.1103/PhysRevMaterials.1.075003.

[8] H. Hazama, M. Matsubara, R. Asahi, T. Takeuchi, Improvement of thermoelectric properties for half-Heusler TiNiSn by interstitial Ni defects, J. Appl. Phys. 110 (2011) 063710. https://doi.org/10.1063/1.3633518.

[9] J.P.A. Makongo, D.K. Misra, X. Zhou, A. Pant, M.R. Shabetai, X. Su, C. Uher, K.L. Stokes, P.F.P. Poudeu, Simultaneous large enhancements in thermopower and electrical conductivity of bulk nanostructured half-Heusler alloys, J. Am. Chem. Soc. 133 (2011) 18843–18852. https://doi.org/10.1021/ja206491j.

[10] A. Page, A. Van der Ven, P.F.P. Poudeu, C. Uher, Origins of phase separation in thermoelectric (Ti, Zr, Hf)NiSn half-Heusler alloys from first principles, J. Mater. Chem. A. 4 (2016) 13949–13956. https://doi.org/10.1039/C6TA04957E.

[11] P.F.P. Poudeu, R. Lu, Y. Liu, P. Sahoo, A. Page, Materials Aspect of Thermoelectricity, CRC Press, Boca Raton : CRC Press, 2017., 2016. https://doi.org/10.1201/9781315197029.

[12] K. Gałązka, S. Populoh, L. Sagarna, L. Karvonen, W. Xie, A. Beni, P. Schmutz, J. Hulliger, A. Weidenkaff, Phase formation, stability, and oxidation in (Ti, Zr, Hf)NiSn half-Heusler compounds, Phys. Status Solidi. 211 (2014) 1259–1266. https://doi.org/10.1002/pssa.201300209.

[13] Y.W. Chai, T. Oniki, T. Kenjo, Y. Kimura, The effect of an isoelectronic Ti-Zr substitution on Heusler nanoprecipitation and the thermoelectric properties of a (Ti0.2,Zr0.8)Ni1.1Sn half-Heusler alloy, J. Alloys Compd. 662 (2016) 566–577. https://doi.org/10.1016/j.jallcom.2015.12.098.

[14] M. Gürth, A. Grytsiv, J. Vrestal, V. V. Romaka, G. Giester, E. Bauer, P. Rogl, On the constitution and thermodynamic modelling of the system Ti–Ni–Sn, RSC Adv. 5 (2015) 92270–92291. https://doi.org/10.1039/C5RA16074J.

[15] M.L.C.C. Buffon, G. Laurita, N. Verma, L. Lamontagne, L. Ghadbeigi, D.L. Lloyd, T.D. Sparks, T.M. Pollock, R. Seshadri, Enhancement of thermoelectric properties in the Nb–Co–Sn half-Heusler/Heusler system through spontaneous inclusion of a coherent second phase, J. Appl. Phys. 120 (2016) 075104.

https://doi.org/10.1063/1.4961215.

[16] Y. Kimura, Y. Tamura, T. Kita, Thermoelectric Properties of Nearly Single-Phase Half-Heusler NbCoSn Alloys and Importance of Microstructures for Improving Performance, MRS Proc. 1044 (2011). https://doi.org/10.1557/proc-1044-u07-06.

[17] Y. Kimura, Y. Tamura, T. Kita, Thermoelectric properties of directionally solidified half-Heusler compound NbCoSn alloys, Appl. Phys. Lett. 92 (2008) 012105. https://doi.org/10.1063/1.2828713.

[18] D. Hull, D.J. Bacon, Introduction to Dislocation, 5th ed., Butterworth-Heinemann, Elsevier, Oxford, 2011.

[19] D.A. Kitchaev, I.J. Beyerlein, A. Van der Ven, Phenomenology of chiral Dzyaloshinskii-Moriya interactions in strained materials, Phys. Rev. B. 98 (2018) 214414. https://doi.org/10.1103/PhysRevB.98.214414.

[20] M.J. Hÿch, L. Potez, Geometric phase analysis of high-resolution electron microscopy images of antiphase domains: Example Cu 3 Au, Philos. Mag. A. 76 (1997) 1119–1138. https://doi.org/10.1080/01418619708214218.

[21] A.P. Pyatakov, A.S. Sergeev, F.A. Mikailzade, A.K. Zvezdin, Spin flexoelectricity and chiral spin structures in magnetic films, J. Magn. Magn. Mater. 383 (2015) 255–258. https://doi.org/10.1016/j.jmmm.2014.11.035.

[22] G. Kresse, J. Furthmüller, Efficiency of ab-initio total energy calculations for metals and semiconductors using a plane-wave basis set, Comput. Mater. Sci. 6 (1996) 15–50. https://doi.org/10.1016/0927-0256(96)00008-0.

[23] Goiri JG, Code, (2019). https://github.com/goirijo/multishifter.

[24] J.P. Perdew, K. Burke, M. Ernzerhof, Generalized gradient approximation made simple, Phys. Rev. Lett. 77 (1996) 3865–3868. https://doi.org/10.1103/PhysRevLett.77.3865.

[25] P. Pochet, B.C. McGuigan, J. Coraux, H.T. Johnson, Toward Moiré engineering in 2D materials via dislocation theory, Appl. Mater. Today. 9 (2017) 240–250. https://doi.org/10.1016/j.apmt.2017.07.007.

[26] Y. Eggeler, E. Levin, F. Wang, R. Seshadri, T. Pollock, D. Gianola, Characterisation

of Misfit Dislocations at Semicoherent Interfaces in Biphasic Functional Heusler Intermetallics, Microsc. Microanal. 25 (2019) 1916–1917. https://doi.org/10.1017/S1431927619010316.

[27] M. De Graef, Introduction to Conventional Transmission Electron Microscopy, Mater. Today. 6 (2003) 57. https://doi.org/10.1016/s1369-7021(03)00636-9.

[28] M.J. Hÿtch, E. Snoeck, R. Kilaas, Quantitative measurement of displacement and strain fields from HREM micrographs, Ultramicroscopy. 74 (1998) 131–146. https://doi.org/10.1016/S0304-3991(98)00035-7.

[29] J.P. Hirth, J. Lothe, Therory of dislocations, 2nd ed., Krieger Publishing company, Malabar Florida, 1982.

[30] L. Kovarik, R.R. Unocic, J. Li, M.J. Mills, The intermediate temperature deformation of Ni-based superalloys: Importance of reordering, JOM. 61 (2009) 42–48. https://doi.org/10.1007/s11837-009-0026-6.

[31] A.E. Gunnæs, S. Gorantla, O.M. Løvvik, J. Gan, P.A. Carvalho, B.G. Svensson, E. V. Monakhov, K. Bergum, I.T. Jensen, S. Diplas, Epitaxial Strain-Induced Growth of CuO at Cu 2 O/ZnO Interfaces, J. Phys. Chem. C. 120 (2016) 23552–23558. https://doi.org/10.1021/acs.jpcc.6b07197.

[32] R.D. Field, T.M. Pollock, W.H. Murphy, The development of y/y' interfacial dislocation networks during creep in Ni-base superalloys, Superalloys 1992, Miner. Met. Mater. Soc. (1992) 557–566.

[33] A. Prakash, J. Guénolé, J. Wang, J. Müller, E. Spiecker, M.J. Mills, I. Povstugar, P. Choi, D. Raabe, E. Bitzek, Atom probe informed simulations of dislocation–precipitate interactions reveal the importance of local interface curvature, Acta Mater. 92 (2015) 33–45. https://doi.org/10.1016/j.actamat.2015.03.050.

[34] Y.B. Bolkhovityanov, L. V Sokolov, Ge-on-Si films obtained by epitaxial growing: edge dislocations and their participation in plastic relaxation, Semicond. Sci. Technol. 27 (2012) 043001. https://doi.org/10.1088/0268-1242/27/4/043001.

[35] G. Gutekunst, J. Mayer, V. Vitek, M. Rühle, Atomic structure of epitaxial Nb-Al2O3interfaces II. Misfit dislocations, Philos. Mag. A Phys. Condens. Matter, Struct. Defects Mech. Prop. 75 (1997) 1357–1382.

https://doi.org/10.1080/01418619708209860.

[36] M. Yamaguchi, Y. Umakoshit, The deformation behaviour of intermetallic superlattice compounds, Prog. Mater. Sci. 34 (1991) 1–148.

[37] M. Yamagiuchi, D.P. Pope, V. Vitek, Y. Umakoshi, Planar faults and dislocation dissociations in body-centred-cubic-derivative ordered structures, Philos. Mag. A. 43 (1981) 1265–1275. https://doi.org/10.1080/01418618108236155.

[38] H. Sehitoglu, J. Wang, H.J. Maier, Transformation and slip behavior of Ni2FeGa, Int. J. Plast. 39 (2012) 61–74. https://doi.org/10.1016/j.ijplas.2012.05.011.

[39] F.B. Mancoff, J.F. Bobo, O.E. Richter, K. Bessho, P.R. Johnson, R. Sinclair, W.D. Nix, R.L. White, B.M. Clemens, Growth and Characterization of Epitaxial NiMnSb/PtMnSb C1 b Heusler alloy superlattices, J. Mater. Res. 14 (1999) 1560–1569. https://doi.org/10.1557/JMR.1999.0209.

[40] W.A. Rachinger, A.H. Cottrell, Slip in crystals of the caesium chloride type, Acta Metall. 4 (1956) 1–19.